

# Chapter 1

## Molecular Movies from Molecular Frame Photoelectron Angular Distribution (MF-PAD) Measurements

Arnaud Rouzée, Ymkje Huismans, Freek Kelkensberg, Aneta Smolkowska, Julia H. Jungmann, Arjan Gijsbertsen, Wing Kiu Siu, Georg Gademann, Axel Hundertmark, Per Johnsson, and Marc J.J. Vrakking

**Abstract** We discuss recent and on-going experiments, where molecular frame photoelectron angular distributions (MFPADs) of high kinetic energy photoelectrons are measured in order to determine the time evolution of molecular structures in the course of a photochemical event. These experiments include, on the one hand, measurements where single XUV/X-ray photons, obtained from a free electron laser (FEL) or by means of high-harmonic generation (HHG), are used to eject a high energy photoelectron, and, on the other hand, measurements where a large number of mid-infrared photons are absorbed in the course of strong-field ionization. In the former case, first results indicate a manifestation of the both the electronic orbital and the molecular structure in the angle-resolved photoelectron distributions, while in the latter case novel holographic structures are measured that suggest that both the molecular structure and ultrafast electronic rearrangement processes can be studied with a time-resolution that reaches down into the attosecond and few-femtosecond domain.

### 1.1 Introduction

Much of our knowledge about matter on the nano-scale is based on studies of the interaction of matter with light. Consequently, the invention of lasers in the infrared, visible and ultra-violet parts of the wavelength spectrum has greatly benefitted our understanding of chemical and physical processes. Using lasers, very insightful ex-

---

A. Rouzée · A. Hundertmark · M.J.J. Vrakking (✉)  
Max-Born Institut, Max Born Straße 2A, 12489 Berlin, Germany  
e-mail: [marc.vrakking@mbi-berlin.de](mailto:marc.vrakking@mbi-berlin.de)

A. Rouzée · Y. Huismans · F. Kelkensberg · A. Smolkowska · J.H. Jungmann · A. Gijsbertsen · W.K. Siu · G. Gademann · A. Hundertmark · M.J.J. Vrakking  
FOM Institute AMOLF, Science Park 104, 1098 XG Amsterdam, The Netherlands

P. Johnsson  
Department of Physics, Lund University, P.O. Box 118, 221 00 Lund, Sweden

R. de Nalda, L. Bañares (eds.), *Ultrafast Phenomena in Molecular Sciences*,  
Springer Series in Chemical Physics 107, DOI [10.1007/978-3-319-02051-8\\_1](https://doi.org/10.1007/978-3-319-02051-8_1),  
© Springer International Publishing Switzerland 2014

periments have become possible, which operate either in the frequency or in the time domain. The latter type of experiment has been particularly informative. Using pump-probe approaches, where a first “pump” laser pulse triggers a structural change in a molecule, and a second “probe” laser pulse interrogates the molecule after it has evolved for some time, detailed questions can be asked that are pertinent to chemical reactivity. The importance of this new research field of “femtochemistry” was recognized by the Nobel Prize in Chemistry that was awarded in 1999 to Prof. Ahmed Zewail (Caltech) [1].

In femtochemistry experiments, information about an evolving molecular structure is typically inferred by measuring how the molecular absorption spectrum (or a related quantity that can be measured, such as a photoelectron or Raman spectrum) changes as a function of pump-probe delay. If it is known how the molecular absorption spectrum depends on the molecular structure, then measuring its time-dependent changes in a pump-probe sequence can inform us about time-dependent structural changes that occur in the molecule. It follows however, that femtochemistry experiments become very challenging when wavelength-dependent spectral features are not very pronounced, or if the relation between the spectrum and the structure is not known ahead of time. Correspondingly, the level of detail that can be extracted from femtochemistry experiments is reduced when the complexity of the molecule increases.

In the last few years a number of new ideas (summarized in Fig. 1.1) have been put forward that aim to remove the above-mentioned limitations of present-day femtochemistry experiments. The common denominator in all these ideas is that they base themselves on diffraction rather than absorption, so that the requirements on pre-existing knowledge of the electronic spectroscopy of the molecule under investigation are significantly relaxed. In a diffraction experiment structural information is encoded in interference patterns that result from the way that an electron or light wave scatters. In the case of light diffraction (see Fig. 1.1a), the required wavelength to resolve interatomic distances is in the X-ray regime. Time-resolved X-ray diffraction was first developed at X-ray synchrotrons, making use of the intrinsic X-ray pulse duration of about 100 ps at typical facilities [2], and was significantly improved by the implementation of slicing facilities where time resolution into the femtosecond regime was accomplished, at the expense of a very significant reduction in the available X-ray fluence [3]. Alternatively, laser-plasma based X-ray sources have been developed that allow performing X-ray diffraction experiments with a time resolution around 100 fs [4]. Finally, time-resolved X-ray diffraction is one of the main driving forces behind the development of X-ray free electron lasers (FELs) like the LCLS at Stanford (which became operational in the fall of 2009 [5]), the SACLA X-ray FEL in Japan and the future European X-ray Free Electron Laser (XFEL) that is under construction in Hamburg. At LCLS, several remarkable results illustrating the potential of coherent diffractive imaging using X-ray FELs have already been achieved [6].

As an alternative to X-ray diffraction, the diffraction of fast electrons can be used. In doing so, an important advantage is the fact that in order for electron wavelengths to match interatomic distances significantly lower electron kinetic en-

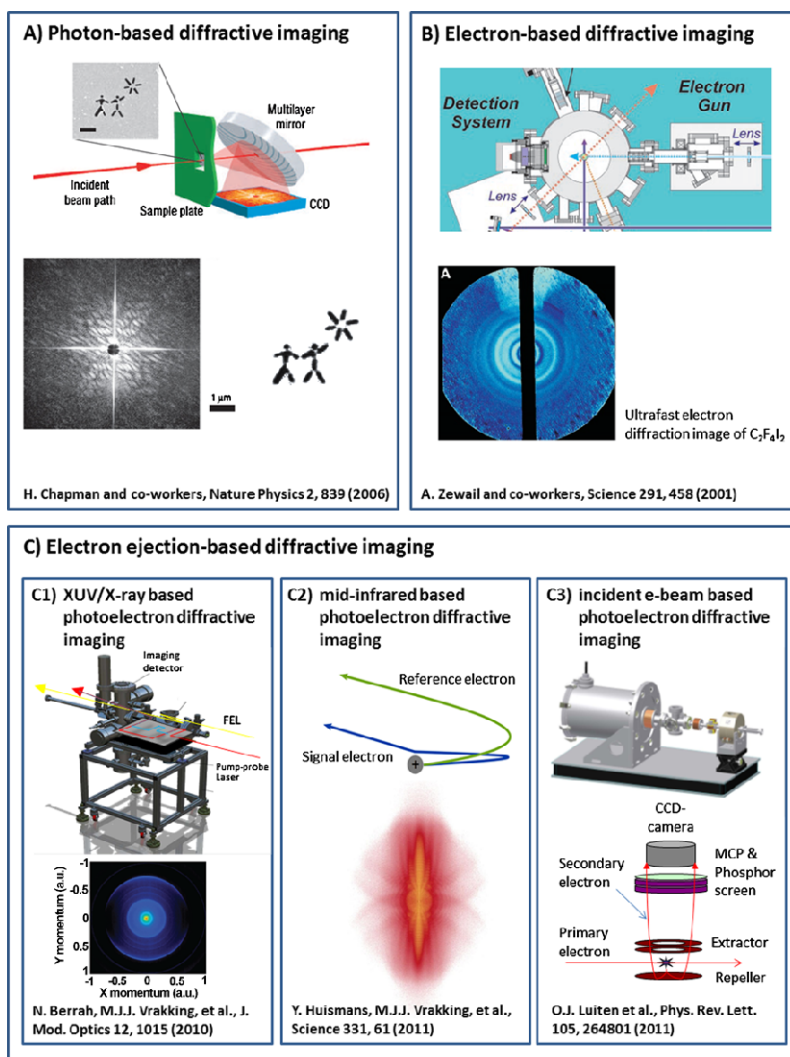


**Fig. 1.1** Compilation of diffractive imaging methods. Methods A and B are based on focusing XUV/X-ray photons from a free electron laser/synchrotron or laser plasma source (A) or an ultra-short, laser-generated electron bunch (B) on a target, and subsequently recording the diffraction of the XUV/X-ray photons and electrons, respectively. In recent years these methods have been successfully implemented. XUV/X-ray diffraction imaging has—in particular—been implemented at FLASH and LCLS, while time-resolved electron diffraction using a photo-cathode source has been implemented in a number of femtosecond laser laboratories. In our research program we aim to develop methodologies for structural determination that are based on measuring diffractive properties of electrons that are extracted from a molecule upon photon or electron impact. In the former case (C1 and C2) ionization is performed using single-photon ionization with an XUV/X-ray laser or multi-photon ionization with a mid-infrared laser. In the latter case (C3) an (e, 2e) or (e, 3e) process is used, where a fast primary electron kicks out a second or even—third electron. An overview of the photon-based experiments (C1 and C2) is presented in this review

ergies are needed than the photon energy of the equivalent X-rays. The de Broglie wavelength of an electron is  $\lambda_{\text{DeBroglie}}(a.u.) = \pi \sqrt{2/E_{\text{kin}}(a.u.)}$ , where  $E_{\text{kin}}$  is the electron kinetic energy. A de Broglie wavelength of  $\sim 1$  Å (which, as a laser wavelength would imply the use of 12.4 keV photons!), is already achieved for electrons with a kinetic energy as low as  $\sim 0.15$  keV. It follows that it is significantly easier to prepare the short pulse electrons that are needed for a time-resolved electron diffraction experiment with atomic resolution, than it is to prepare the short pulse X-rays that are needed for a time-resolved X-ray diffraction experiment.

Short electron pulses with kinetic energies in the 0.1–1000 keV range can be generated externally to a molecule on a photo-cathode that precedes a small accelerator. Using such a technique impressive results have been achieved by Zewail and co-workers [7–9] and by Miller and co-workers (see Fig. 1.1b) [10]. Applications have included studies of halo-ethane elimination reactions and ring opening of cyclic hydrocarbons [7], phase transitions in cuprate semiconductors [9], the transition from a monoclinic to a final tetragonal phase in crystalline vanadium dioxide [8], and laser-induced melting [10]. Already, these experiments can be performed with a time resolution of approximately 100 femtoseconds. It remains to be seen if pump-probe experiments with ca. 10 femtosecond time-resolution will become possible using this technique, although proposals to push the time resolution into the attosecond domain have already been put forward [11].

In the last few years, our research team has started working on a number of alternative methods that allow the generation of electrons with kinetic energies in the 0.1–1 keV range, two of which will be detailed in this book chapter (see Fig. 1.1c). First of all, in experiments performed at extreme ultra-violet (XUV)/X-ray FELs like the FLASH free electron laser in Hamburg (the pre-cursor of the European XFEL, which generates radiation down to 4 nm) and at LCLS, we have explored the generation of fast electrons by XUV/X-ray photo-ionization as a means to study time-resolved molecular dynamics. Like the time-resolved X-ray diffraction studies mentioned above, this work may be seen as a natural continuation of earlier synchrotron-based experiments, where ideas to use XUV/X-ray radiation for “illuminating a molecule from within” were developed about a decade ago [12, 13]. A progress report on the extension of these ideas to the time domain will be presented below. Secondly, in experiments performed at the mid-infrared free electron laser FELICE (Free Electron Laser for Intra-Cavity Experiments) in the Netherlands, we have investigated strong-field ionization at wavelengths ranging between 4 and 40  $\mu\text{m}$ . Under these conditions, considerable ponderomotive acceleration of the electrons that are freed in the ionization event sets the stage for laser-driven re-collisions with the target from which the electrons are ionized, allowing the experimental measurement of photoelectron holograms that encode both molecular structure and dynamics [14]. These experiments are discussed in the present chapter as well. We note that in future we are furthermore planning experiments where 0.1–1 keV electrons that can encode molecular structures will be ejected from (time-evolving) molecules by means of a collision of the molecule with a 100 keV electron beam that is similar to the elec-

tron beams that are used for the ultrafast electron diffraction experiments mentioned above [15]. The key difference here will be that the diffractive information is to be encoded in the ejection of secondary or tertiary electrons from the molecule, rather than onto the diffraction of the incident high-energy electron beam.

The organization of the present chapter is as follows. In Sect. 1.2 we present our efforts on using XUV/X-ray single-photon ionization as a means to generate fast photoelectrons that encode a (time-evolving) molecular structure. We present the status of our work at FLASH and LCLS, where we have performed alignment-pump-probe experiments, where a first, alignment laser pulse dynamically aligns the molecule under investigation, a pump laser pulse photo-excites the molecule and the FEL pulse ionizes the molecule at a variable time delay, as well as recent experiments where a high-harmonic generation (HHG) source was used to generate a comb of XUV laser frequencies reaching up to 50 eV, and where photoionization of a series of small molecules provided insight into the contribution of different molecular orbitals and the onset of the emergence of structural information. In Sect. 1.3 we present results from our experiments on (atomic) strong field ionization at mid-infrared wavelengths ranging from 4 to 40  $\mu\text{m}$ , where holographic interferences in the measured photoelectron momentum distributions suggest a route towards a novel technique for measuring (time-resolved) molecular, structural information.

## 1.2 Molecular Movies Using XUV/X-Ray Photoionization

In the last few years two novel XUV/X-ray short-pulse light sources have come to the forefront that have significantly changed the opportunities that experimentalists in atomic and molecular physics research can avail themselves of. On the one hand, HHG has been developed into a technique that can be implemented in moderate-scale laser laboratories on the basis of commercially available, mJoule-level, femtosecond lasers [16–18]. When the pulses from these lasers are focused onto a dense, gas phase, atomic or molecular target, XUV/X-ray light pulses are formed by means of an interaction that is commonly described in terms of a three-step mechanism, where the laser first ionizes the atom/molecule under consideration, then accelerates the ionized electrons and finally drives the electron back towards the ion left behind, where a recombination can occur that is accompanied by the emission of XUV/X-ray light [19]. Since this process repeats for every half-cycle of the driving laser field, the output frequencies are restricted to odd harmonics of the driver laser frequency, explaining the name of the technique. On the other hand, several XUV/X-ray FEL user facilities have recently become available that provide femtosecond XUV/X-ray pulses with pulse energies that are well beyond the reach of present-day HHG schemes. The first examples of such facilities have been the Tesla Test Facility (TTF) and FLASH in Hamburg [20]. More recently, the LCLS at Stanford has come into operation as the world's first hard X-ray FEL user facility [5].

The interest in the use of these novel XUV/X-ray light sources in atomic and molecular physics can be rationalized both in the time and frequency domain. Viewed in the time domain, the inherently short optical periods of XUV/X-ray light ( $\tau_{\text{optical}} = \lambda/c$ , where  $\lambda$  is the wavelength and  $c$  is the speed of light), allows the synthesis of pulses with unprecedented pulse durations, accessing the sub-femtosecond i.e. attosecond domain [17, 18, 21]. Such pulses are ideal for the investigation of electron dynamics on its natural timescale. The generation of attosecond laser pulses requires the availability of a process that generates light in the XUV/X-ray regime over a large enough bandwidth ( $\Delta E \geq 5$  eV) and with an appropriate phase relationship between the different frequency components contained within the pulse. This is precisely what the HHG process does, given the one-to-one relationship between the ionization time within the optical cycle of the driving infrared laser, the kinetic energy at the time of the electron-ion re-collision and the photon energy produced. Under typical HHG conditions, XUV/X-ray bandwidths in excess of 20 eV are easily achieved, and the pulse duration is determined by the chirp that is generated in the HHG process. The shortest pulses reported to date are about 80 attoseconds long [22], and it is to be expected that the existence of even shorter pulses will soon be demonstrated. So far, pulses obtained at XUV/X-ray FELs are still in the femtosecond domain, but ideas exist that would allow to significantly shorten the pulses [23]. At LCLS, X-ray laser pulses with a pulse duration below 10 fs have already been achieved [24].

Viewed in the frequency domain, the short wavelength and thus intrinsic high photon energy of XUV/X-ray light sources creates the ability to produce high energy photoelectrons. As we will discuss, this allows configuring molecular pump-probe experiments where photoelectrons are produced with kinetic energies where the de Broglie wavelength becomes comparable to or smaller than the internuclear distances in the molecule, so that the angular distribution of the ejected photoelectron encodes information on the molecular structure. Mentioning the time domain, attosecond science context is highly relevant here, since the intensive and widespread efforts to develop and characterize attosecond light pulses have largely been responsible for the emergence of the experimental protocols that need to be used when MFPADs are to be measured using XUV/X-ray light generated by HHG. Motivated by the requirements for attosecond science experiments, it has become possible to develop interferometrically stable multi-color pump-probe setups, with appropriate optics that can be used to image, focus, split and recombine the XUV/X-ray light beam. An example of such a setup is shown in Fig. 1.2 and corresponds to the setup that is in operation at the Max Born Institute (MBI) in Berlin.

If one wishes to time-resolve the evolution of internuclear distances in a molecule (in other words, make a “molecular movie”) using photoelectrons that are ejected from the molecule using XUV/X-ray light, then it is imperative that the photoelectron angular distribution is observed in the molecular frame. One way to do this is by making use of a so-called reaction microscope [25], where the 3D momentum of ejected photoelectrons is measured in coincidence with the 3D momentum of fragment ions that are formed, and where in the axial recoil approximation the lat-

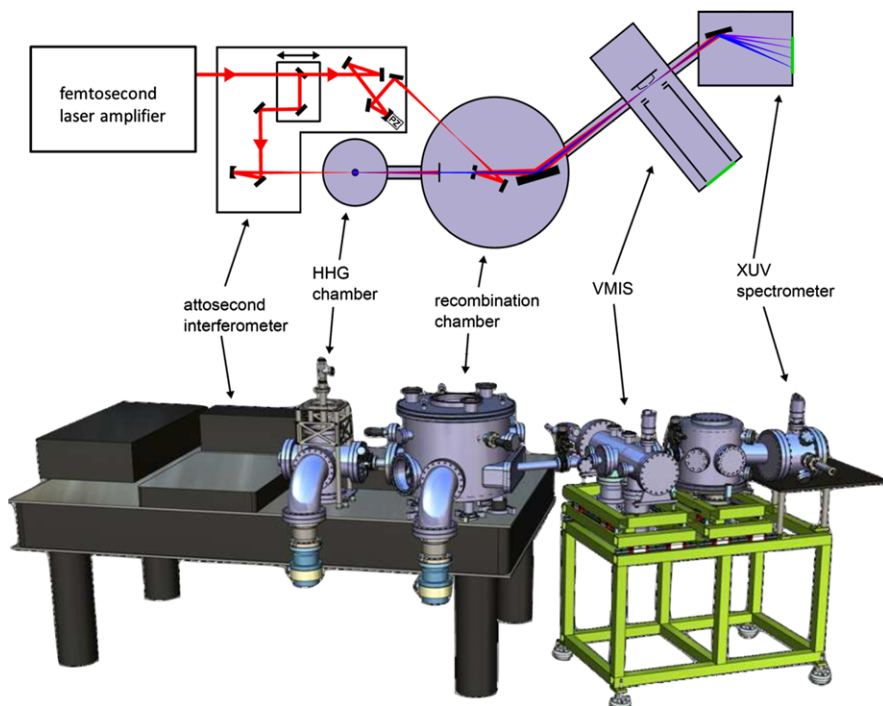


**Fig. 1.2** The attosecond pump-probe setup at the Max-Born Institute (MBI). The output of a Ti:Sa laser is split into two beams, that form the two arms of a Mach-Zehnder interferometer. In one arm the laser is focused into a HHG gas cell. Following the HHG process and removal of the IR light and the generated low-order harmonics by means of a filter, this arm is recombined with the other arm in a recombination chamber. The co-linearly propagating XUV and IR beams are brought to a common focus in the center of a velocity map imaging spectrometer (VMIS) by using a toroidal mirror. Finally, an XUV spectrometer that follows the VMIS monitors the harmonic spectrum. In the experiments presented in this chapter, the IR beam was used to dynamically align  $\text{CO}_2$ ,  $\text{O}_2$ ,  $\text{N}_2$  and  $\text{CO}$  molecules. The XUV ionized the aligned molecules, and the VMIS was used to record angle- and energy-resolved photoelectrons and fragment ions resulting from this ionization process

ter allow to determine the 3D orientation of the molecule at the time of ionization. A disadvantage of the use of reaction microscopes is the fact that the coincidence requirements imply that at most one electron-ion pair can be measured per laser shot, meaning that at the typical kHz repetition rates of HHG driver lasers the total amount of time needed to perform an experiment becomes prohibitive. Therefore, in our research we have focused our attention on another approach, namely one where a macroscopic molecular sample is dynamically aligned prior to the pump-probe experiment by means of the interaction with a short alignment laser pulse. By dynamic alignment we understand the re-orientation of a molecule in the laboratory frame that results from the torque that an intense laser field exerts on the molecule as a result of the interaction of the laser-induced dipole with the laser field [26]. Two



distinguishable variants exist, namely adiabatic alignment, where the molecule is exposed to a laser pulse that is significantly longer than the rotational period of the molecule [27], and impulsive alignment, where the molecule is exposed to a laser pulse that is significantly shorter than the rotational period [28]. The advantage of the latter method is that it leads to the formation of aligned molecular samples under laser field-free conditions (i.e. after the alignment laser pulse is over), although with a degree of alignment that is lower than in the adiabatic case. Hybrid schemes combining adiabatic and impulsive alignment have also been proposed [29], and—in combination with state-selection techniques—allow the preparation of molecular samples with a very high-degree of alignment and orientation [30] that can be used in experiments aimed at observing the emission of photoelectrons in the molecular frame.

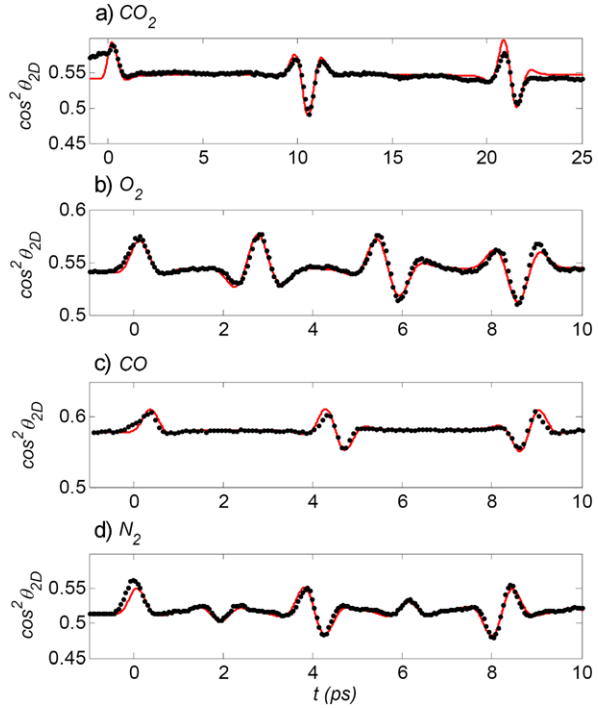
Recently the experimental setup shown in Fig. 1.2 has been used to perform such an experiment [31]. A series of small molecules ( $\text{CO}_2$ ,  $\text{N}_2$ ,  $\text{O}_2$  and  $\text{CO}$ ) were exposed to the sequence of an IR laser pulse that dynamically aligned the molecules and an XUV pulse generated by HHG that ionized the molecules at a variable time delay. Photoelectrons and fragment ions resulting from the latter photoionization process were recorded on a velocity map imaging detector, i.e. accelerated towards a two-dimensional detector consisting of a set of micro-channel plates, a phosphor screen and a CCD camera, thereby allowing the measurement of a 2D projection of the 3D velocity distribution. The 3D velocity distribution was determined from the 2D projection by means of an iterative Abel inversion routine [32]. An important feature of the experiment was the fact that a very high count rate could be achieved (up to ca.  $10^6$  counts/second), due to the use of a very efficient gas injection system, which was integrated in the repeller electrode of the velocity map imaging spectrometer [33]. This allowed achieving very high signal-to-noise ratios in the data acquisition, which were crucial for observing the small differences in the photoelectron angular distribution of aligned and non-aligned (or anti-aligned) molecules.

Figure 1.3 provides an overview of the dynamic alignment that was achieved in the experiment. The experimental angular distributions of high energy  $\text{O}^+$ , resp.  $\text{N}^+$  fragments resulting from XUV-induced dissociative ionization and/or Coulomb explosion are plotted as a function of the time delay between the impulsive alignment by the IR laser and the XUV ionization by the HHG laser. The angular distributions are expressed by means of  $\langle \cos^2 \theta_{2D} \rangle$ , where  $\theta_{2D}$  is the angle between the measured velocity of the fragment ion in the plane of the 2D detector and the common polarization axis of the XUV and IR beams. Perfect alignment of the molecular axes corresponds to  $\theta_{2D} = 0$ , whereas  $\theta_{2D} = \pi/2$  corresponds to molecules that are anti-aligned, i.e. having their internuclear axis perpendicular to the polarization axis of the alignment laser.  $\theta_{2D}$  is not to be confused with  $\theta$ , the angle between the 3D fragment ion velocity and the laser polarization axis. The degree of molecular alignment is given by  $\langle \cos^2 \theta \rangle$ .

As Fig. 1.3 shows, an IR-laser induced alignment occurs shortly after the excitation by the IR laser pulse, and is then followed by a series of alignment revivals



**Fig. 1.3** (a)–(d) Experimental (black dots) and theoretical (red lines) alignment of CO<sub>2</sub>, O<sub>2</sub>, CO and N<sub>2</sub>, as a function of the time delay between the IR alignment laser and the XUV ionization laser. The numerical calculations are based on the method described in [65] and allow a determination of the rotational temperature of the molecular sample and the average intensity of the IR beam in the XUV focus



that occur at regular time intervals determined by the rotational constants of the molecules under investigation. The approximately 300 fs long IR laser pulse imparts a kick on a timescale that is short compared to the rotational period of the molecule (i.e.  $\tau_{\text{laser}} \ll \tau_{\text{rot}}$ ). Consequently, a rotational wave packet is formed that evolves under field-free conditions once the alignment laser field has ended and that periodically re-aligns and anti-aligns due to the re-phasing of the rotational components. The maximum degree of alignment in Fig. 1.3 corresponds to  $\langle \cos^2 \theta \rangle \approx 0.5$ , and is not very high. This is due to the finite rotational cooling experienced by the gas leaving the capillary in the repeller electrode. Fitting of the experimental alignment distributions to theoretical results (red curves in Fig. 1.3) suggests a rotational temperature ranging from 75 K for the case of CO<sub>2</sub> to 37 K for the case of N<sub>2</sub>. However, the achieved difference in the alignment and anti-alignment is sufficient for obtaining high quality differential photoelectron distributions that are acquired by taking the difference between a photoelectron measurement at a delay where the molecules are maximally aligned, and one at a delay where the molecules are maximally anti-aligned. The result of this procedure is shown for CO<sub>2</sub> in Fig. 1.4. Figure 1.4a first of all shows a 2D slice through the 3D XUV-only photoelectron kinetic energy and angular distribution that is measured without the IR-alignment laser. A large number of rings are observed due to the participation of harmonics H11–H29 in the experiment, as well as the fact that at least 4 orbitals contribute to the ionization (the HOMO ( $X^2\Sigma_g$ ,  $IP = 13.8$  eV), the HOMO-1 ( $A^2\Pi_u$ ,  $IP = 17.6$  eV), the HOMO-2 ( $B^2\Sigma_u$ ,  $IP = 18.1$  eV) and the HOMO-3

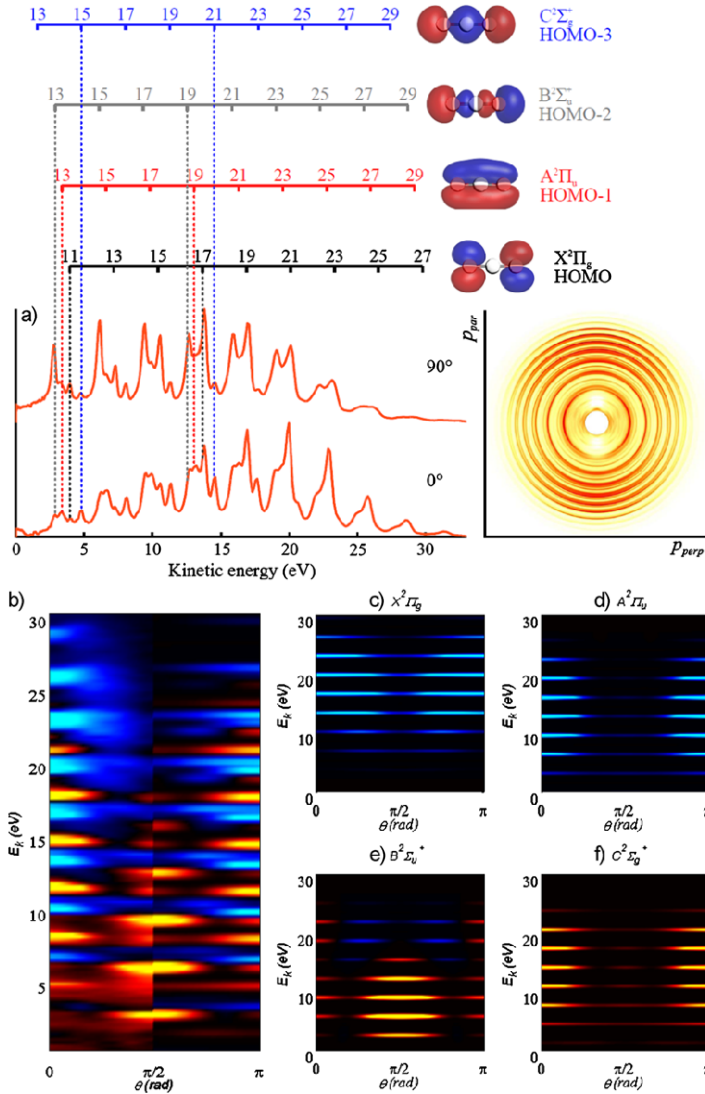


**Fig. 1.4** (a) XUV-only ionization of CO<sub>2</sub>, involving contributions from harmonics H11 to H29. The *bottom left panel* shows a 2D slice through the 3D photoelectron momentum distribution obtained after Abel inversion of the experimental data. The *bottom right panel* shows the integrated photoelectron spectrum along (*top*) and perpendicular (*bottom*) to the laser polarization; (b) comparison between the experimental and theoretical differential angular and kinetic energy distribution that is obtained by taking the difference between the photoelectron momentum distributions obtained for maximally aligned and maximally anti-aligned CO<sub>2</sub> molecules; (c–f) calculated evolution of the differential photoelectron angular distributions as a function of the photoelectron kinetic energy, for the four ionization channels observed in the experiment. (*Light*)*blue color* means a negative value, implying that the efficiency for signal for aligned molecules is less than that for anti-aligned molecules, whereas *red/yellow color* implies a positive value, implying that the signal is increased when the molecule is aligned

( $C^2\Sigma_g$ ,  $IP = 19.4$  eV)). When the ionization by the XUV laser pulse is preceded by the IR alignment laser, appreciable changes occur in the measured photoelectron momentum distributions. This is reflected in the experimental contour plot (left side) shown in Fig. 1.4b, where the afore-mentioned differential photoelectron kinetic energy and angular distribution is plotted as a function of the kinetic energy and the angle of ejection of the photoelectron with respect to the laser polarization axis. The differential photoelectron kinetic energy and angular distribution shows all the rings that are visible in the 2D slice in Fig. 1.4a, and moreover shows that the differences between the measurements for aligned and anti-aligned molecules sensitively depend both on the orbital that is ionized and the electron kinetic energy. To begin with, the influence of the ionized orbital manifests itself in the total photoelectron yield. The yield of electrons from the HOMO and HOMO-1 orbitals is suppressed when the molecules are aligned compared to when the molecules are anti-aligned, whereas the yield of photoelectrons corresponding to the HOMO-3 increases when the molecules are aligned. Ionization of the HOMO-2 favors aligned molecules at low photoelectron kinetic energies, but this behavior reverses above a kinetic energy of 15 eV, when anti-aligned molecules ionize more efficiently.

The dependence of the ionization on the alignment/anti-alignment of the molecular sample informs about the perpendicular resp. parallel character of the ionizing transition. When the photoionization occurs by means of a parallel transition the ionization efficiency of molecules that are aligned parallel to the laser polarization axis will be higher than that of molecules that are anti-aligned. In this case, the symmetry of the final (molecular ion + electron) state will be  $\Sigma_u$ . Similarly, when the photo-ionization occurs by means of a perpendicular transition, the ionization efficiency of molecules that are aligned perpendicular to the laser polarization axis will be higher than that of molecules that are aligned along the polarization axis and the symmetry of the final (molecular ion + electron) state will be  $\Pi_u$ . Based on the experimental data the conclusion can be drawn that the HOMO and HOMO-1 of  $\text{CO}_2$  ionize by means of a perpendicular transition, and the HOMO-3 by means of a parallel transition. The ionization of the HOMO-2 is predominantly parallel at low energies (up to a photoelectron kinetic energy of 15 eV) and then changes to predominantly perpendicular.

The experimental results can be well-reproduced by an electron-molecule quantum scattering method that was previously also successfully applied to calculate MFPADs recorded with synchrotron radiation [34, 35]. This method is based on the multichannel Schwinger configuration interaction method (MCSCI), where the initial state and the final ionic states are represented as configuration interaction (CI) wave functions. Calculated differential photoelectron kinetic energy and angular distributions (making use of the alignment distributions provided by the experimental fits of the time-dependent molecular alignment, see Fig. 1.3) are shown in the contour plot shown on the right side of Fig. 1.4b, as well as in Figs. 1.4c–f, where the theoretical differential photoelectron kinetic energy and angular distributions are plotted separately for the four most important orbitals that contribute to the ionization signal. The overall agreement between the experimental and theoretical data is very satisfactory.

In the final (molecular ion + electron) state the symmetry of the wavefunction is determined both by the electronic state of the ion and that of the continuum electron. The wave function of a photoelectron ejected by single photon ionization can be expressed as a superposition of partial waves that are characterized by the angular momentum  $l$  of the photoelectron and a symmetry index  $\lambda$  that describes the projection of this angular momentum on the molecular axis; for  $\lambda = 0$  the states are designated as  $\sigma$  and for  $\lambda = 1$  as  $\pi$ . In practice, the partial-wave expansion converges at relatively small  $l$  ( $l < 4$ , or in usual notation s, p, d and f partial waves). In addition, the dipolar  $u \longleftrightarrow g$  selection rule restricts the electron in the continuum to ungerade symmetry for the final ionic states  $X^2\Sigma_g$  and  $C^2\Sigma_g$  (which implies that only odd angular momenta appear in the partial wave expansion of the outgoing electron) and to gerade symmetry for the final ionic states  $A^2\Pi_u$  and  $B^2\Sigma_u$  (which means that only even angular momenta appear in the partial wave expansion of the outgoing electron). One cannot extract the partial wave decomposition of the electronic wave packet from the experimental results due to the low degree of alignment. The experimental result can only put constraints on the possible decomposition of the electronic wavepacket into partial waves. For the ionization leading to the final  $X^2\Sigma_g$  ground ionic state for instance, where the wave packet is mainly composed of  $l = 1, 3$  (p and f waves), the pronounced positive contribution along the laser polarization axis that is observed both theoretically and experimentally suggests that the photoelectron partial wave decomposition contains a strong contribution from the p-partial wave. The computational results support this notion, but also suggest an important role for f-wave photo-emission.

One of the most significant results that follows from the experimental and theoretical contour plots shown in Fig. 1.4b–f is the fact that the differential photoelectron angular distributions clearly depend on the kinetic energy of the outgoing electron. This may be interpreted as a manifestation of the onset of structural information in the photoelectron angular distributions. Although the photoelectron kinetic energies are still too low to observe readily interpretable diffraction patterns, and although the differential photoelectron angular distributions are heavily affected by the extensive angular averaging that occurs as a result of the rather modest degree of alignment and anti-alignment in the experiment, this result provides the rationalization for attempts to extend these results to higher photon energies. Extending the use of HHG sources, this may become possible in the near future by the use of different generating gasses with a higher cut-off (He or Ne, rather than Ar) in the HHG process [36], and/or by performing HHG with a longer wavelength driver wavelength [37] or making use of a multi-color field [38].

Alternatively, higher photon energies may be accessed by performing the experiment at one of the emerging XUV/X-ray FEL facilities, which moreover have the advantage that they offer a peak brightness which exceeds that of HHG sources by many orders of magnitude. FELs like FLASH and LCLS offer more than  $10^{12}$  photons/pulse at photon energies ranging from ca. 0.04 to 10 keV. However, the advantages of FELs over HHG come at the expense of a lack of coherence and the difficulty to synchronize other laser sources to the FEL. The former is not a serious problem in molecular pump-probe experiments aiming at femtosecond time resolution,

whereas the latter implies that in experiments requiring high time-resolution additional measurements (e.g. electro-optical measurements [39] or cross-correlation schemes based on transient X-ray induced reflectivity modification [40]) are needed to measure the jitter between the FEL and a 2nd laser on a shot-by-shot basis. Moreover, the development of new protocols is required that allow to find the temporal and spatial overlap of the FEL laser beam and the other laser beam(s) that are used in the experiment. The availability of a velocity map imaging spectrometer provides very useful opportunities for doing this, given that the detector can be used both in a spatial and a velocity map imaging mode, while at the same time providing high quality time-of-flight information [41].

The alignment-pump-probe approach with velocity map imaging detection of high energy photoelectrons described above is in principle very suitable for application at FELs. In contrast with the use of a reaction microscope, the velocity map imaging technique allows the recording of rather large signals before space-charge distortions of the measured angular and velocity distribution set in. For example, when an FEL is focused to a spot diameter of about 100  $\mu\text{m}$  and intersects the molecular beam containing the target molecules over a length of about 1 mm, then as many as  $10^3$  photoelectrons can be generated and measured per laser shot, before one exceeds the empirical threshold of ca.  $10^8$  photoelectrons/ $\text{cm}^3$  where space charge effects start to cause serious problems.

Our first activity at the FLASH FEL was to introduce the use of velocity map imaging (VMI) [42, 43]. As far as the use of XUV/X-ray photoionization for the time-resolved observation of molecular dynamics is concerned, we have so far developed an alignment-pump-probe experiment where small molecules like  $\text{Br}_2$  are dynamically aligned using the fundamental 800 nm wavelength of a Ti:Sa laser, photo-dissociated using the 2nd harmonic of this laser [44] and then ionized by the FEL. Figure 1.5(a)–(c) shows 2D momentum maps of  $\text{Br}^{2+}$  fragments in the presence of only the FEL (a), with both the 400 nm and the FEL beam present (b), and when all three pulses are present (c) [45, 46]. In the presence of the FEL pulse, the 2D velocity distribution is composed of concentric rings originating from dissociative ionization and Coulomb explosion of the molecule. The prominent new contribution observed in Fig. 1.5(b) results from the ionization by the FEL pulse of fragments of the dissociation initiated by the 400 nm pulse. When adding the 800 nm pulse, the angular distribution peaks along the laser polarization axis (see Fig. 1.5(c)), which indicates that the molecules are aligned prior to dissociation and ionization. First attempts have been made to record photoelectron angular distributions under these conditions. Figure 1.5(d) shows a differential photoelectron momentum map similar to the data shown in Fig. 1.4, where in the present case the difference is shown between a photoelectron momentum map recorded before and after dissociation by the 400 nm photo-excitation laser pulse. From the difference image a clear signature of the result of the dissociation process can be identified through the shift of the resulting photoelectron energies and changes in the angular distribution of photoelectrons from the 3d shell. Recording of photoelectron data with the time resolution required for a complete investigation of the  $\text{Br}_2$  dissociation dynamics has not been completed yet.

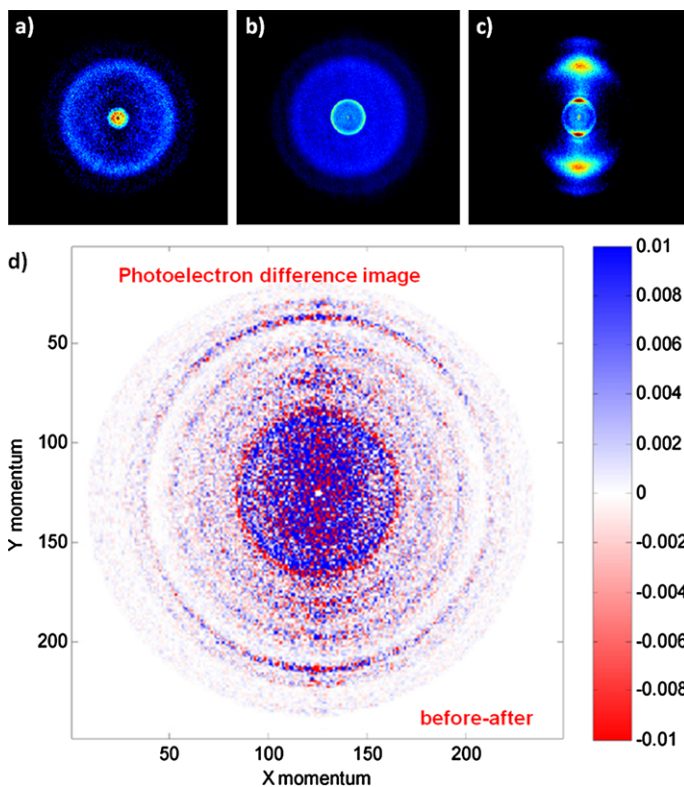


**Fig. 1.5** (a)–(c)  $\text{Br}^{2+}$  ions resulting from dissociative ionization of  $\text{Br}_2$  by 13 nm light from FLASH. In (a), the FEL pulse alone is impinging on the molecules, resulting in fragmentation through dissociative ionization (central ring) or Coulomb explosion (outer two rings). In (b), the FEL pulse is preceded by a 400 nm pump pulse which induces dissociation of the neutral molecule, resulting in a sharp central ring. In (c), an IR alignment pulse is sent in 1 ps before the other two pulses, impulsively aligning the molecule and resulting in a momentum distribution that is peaked along the laser polarization axis; (d) differential photoelectron momentum map, showing the difference between a photoelectron map for dissociated and non-dissociated  $\text{Br}_2$  molecules

### 1.3 Molecular Movies Using Strong Field Mid-Infrared Ionization

In the experiments described in the previous section, high-energy electrons were generated by high energy XUV/X-ray single photon ionization. However, this is not the only way that electrons can acquire a high kinetic energy. Alternatively, electrons can be accelerated to high kinetic energies using ponderomotive acceleration in an intense laser field. In this case the energy acquired by the electron scales with  $I_{\text{laser}}\lambda_{\text{laser}}^2$ , where  $I_{\text{laser}}$  is the intensity of the laser and  $\lambda_{\text{laser}}$  is the laser wavelength. It follows that ponderomotive acceleration is particularly relevant for lasers operating in the mid-infrared wavelength range.

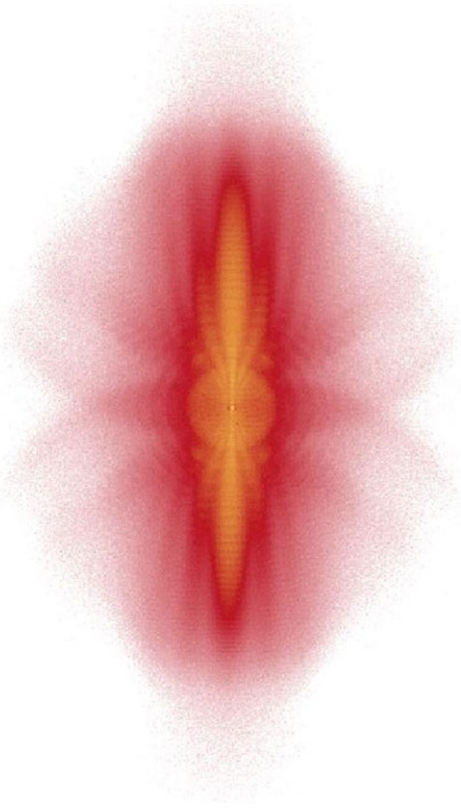
The use of mid-infrared strong-field ionization as a means of probing molecular dynamics is a research field that is only now being first attempted in a number of laboratories. However, there exists already a highly relevant body of work concerned with how HHG, beyond its use as a source of coherent XUV light, can be used to study atomic and molecular structure and time-resolved dynamics, by measuring the harmonic emission as a function of molecular alignment. These experiments, which have come to be known as “orbital tomography” or “harmonic imaging” experiments, probe the molecular structure since they are sensitive to multi-particle interference effects [47], and allow to re-construct the amplitude and phase of the orbital from which the ionized electron was removed [48]. Of particular interest have also been recent experimental and theoretical works showing that attosecond time-scale electron dynamics in molecular ions can be probed [49], as well as experiments where the breaking of a molecular bond was followed by monitoring the harmonic emission from the dissociating molecule as a function of time [50].

In the harmonic imaging experiments, the available observables are typically the amplitude and phase of a limited number (typ. 5–10) of harmonics. Alternatively, outcomes of the electron-ion re-collision that do not involve photon emission, but where the electron elastically or inelastically scatters off the ion, can be measured. Measurements of 2D photoelectron momentum distributions in principle provide a very rich observable, since every distinguishable final momentum of the electron ( $p_z$ ,  $p_x$ ), where  $p_z$  is the momentum along the polarization axis and  $p_x$  the momentum orthogonal to it, may be viewed as an independent measurement. Scattering of re-collision electrons from different constituent atoms within a molecule may lead to diffraction patterns characterized by constructive and destructive interferences that appear at specific final momenta [51, 52]. In addition, the interference between scattered and non-scattered, laser-ionized electrons leads to holographic interferences that provide further opportunities for the retrieval of dynamical and structural information.

The first experimental observation of the above-mentioned holographic interference structures was recently made in an experiment where metastable Xe atoms were ionized using 7  $\mu\text{m}$  radiation from the FELICE FEL at Rijnhuizen in the Netherlands (see Fig. 1.6) [14]. 2D photoelectron momentum maps were measured with the help of a velocity map imaging spectrometer that was integrated into the FEL cavity. Under the influence of the FEL the outermost electron is pulled out of the atom along the polarization axis and starts an oscillatory motion in the laser field. The outer turning point of this oscillatory motion can be viewed as an electron source (at a distance of about 20 Angströms from the atom!) from which electron waves are emitted that reach the detector either with or without interacting with the ion from which they are produced. In the former case we are justified in thinking of the electron wave as a signal wave that encodes information about the ion, while in the latter case we are justified in thinking of the electron wave as a reference wave. In this sense, the experiment records a hologram that can in principle be used to retrieve information about the atomic or molecular target from which the electron was extracted.



**Fig. 1.6** Cut through the 3D photoelectron momentum distribution recorded for the ionization of metastable Xenon atoms by 7  $\mu\text{m}$  FELICE radiation, showing the appearance of side-lobes that result from a holographic interference between electrons that scatter off the  $\text{Xe}^+$  ion and electrons that do not. In the image, the *vertical axis* corresponds to the polarization axis of the FELICE free electron laser. The peak intensity of the FELICE laser was  $7 \times 10^{11} \text{ W/cm}^2$ . The image shown here is the result of a 4-hour long measurement. The dynamic range in the image extends over 4 orders of magnitude



The observation of photoelectron holograms in strong-field ionization at mid-infrared wavelengths was quite unexpected, since prior to the experiment the conventional wisdom in the strong-field laser community was that with substantial scaling of the laser wavelength towards the mid-infrared the efficiency of the electron-ion re-collision would dramatically diminish. This is the reason, for example, why it is experimentally observed that the efficiency of HHG drops as function of driver wavelength with approximately  $\lambda^{-(5-6)}$ . However, the recent results that we have obtained at FELICE have shown that, as a result of Coulomb focussing of the electron trajectories, substantial re-collision amplitudes remain observable for wavelengths as long as 40  $\mu\text{m}$  (!), where holograms such as the one shown in Fig. 1.6 could readily be observed. It is noteworthy that the photoelectron holograms observed in strong-field ionization are strongly related to interferograms that we have observed about a decade ago in velocity map imaging experiments on threshold photoionization of atoms in a weak DC electric field [53, 54]. In this case the interferences are caused by the fact that in a DC electric field there exist an infinite number of classical trajectories connecting the atom and a particular point on the detector, differing in the number of returns of the electron to the ionic core prior to ionization. Similarly, in the present strong-field holography case there are—in principle—an infinite number of trajectories that differ in the number of times that a laser-driven glancing re-

collision takes place. Evidence for the occurrence of multiple/late re-collisions was explicitly observed in [14]. The late re-collisions correspond to trajectories where the electron, after being pulled out of the atom in a particular half-cycle, misses the ion on the first, or even second re-collision opportunity, so that the scattering event that leads to a substantial change in the electron momentum only occurs on the second, or even third re-collision opportunity.

The hologram in Fig. 1.6 can on the one hand be viewed as a ‘static’ measurement with the potential to determine a molecular structure. Since, however, this measurement is completed within the pulse duration of the mid-infrared ionization laser, it can be easily extended to the monitoring of time-dependent structural changes in molecules, provided that the mid-infrared laser sources can be constructed with a pulse duration that is commensurate with the time-dependent molecular structural changes of interest. With the availability of 30–50 fs mid-infrared laser pulses these two requirements can readily be reconciled. At the same time, a single hologram such as shown in Fig. 1.6 already contains time-dependent information on ultrafast electron dynamics, due to the way that the time of ionization and the time of the re-collision with the ion directly determine the final momentum. This is very similar to the operating principle of the attosecond streak camera, that is commonly used in attosecond science to characterize attosecond laser pulses and to record time-dependent events on the attosecond timescale [55, 56]. In this manner, the holography experiment allows to obtain information on the ionization dynamics and ultrafast ‘hole dynamics’ in the molecular ion left behind that is on the sub- or few-femtosecond timescale.

In order to arrive at the interpretation of the side-lobes in Fig. 1.6 in terms of a holographic interference between a signal and reference electron wave, a number of numerical methods were used. The side-lobes are reproduced when the time-dependent Schrödinger equation (TDSE) is solved in the single active electron (SAE)-approximation [57], but this does not provide any physical insight yet. A deeper understanding can be obtained when using methods that are based on the strong-field approximation (SFA), which has already been invoked in the explanation of many strong-field phenomena [58]. In the SFA, one assumes that prior to ionization the laser field has a negligible interaction with the electron compared to the interaction of the electron with the atomic or molecular ion core, and that after ionization, which is assumed to occur by means of a tunneling process, the situation is reversed, i.e. the motion of the electron is then entirely governed by the interaction of the electron with the laser field. These assumptions allow one to explain, for example, the high-energy cut-off that is observed in HHG [19]. SFA in its simplest form cannot explain the holographic interferences that are observed in Fig. 1.6, since it does not include the Coulomb interaction of the electron with the ion from which it is extracted and the changes in the electron momentum that are induced by electron-ion recollisions that occur under the influence of the oscillatory laser field. A suitable method to include the Coulomb interaction into SFA was introduced by Bauer and Prophuzhenko [59, 60], making use of the fact that within an SFA framework strong field ionization can be numerically evaluated using the application of a saddle-point method [61], which regards ionization resulting in a given final momentum ( $p_z$ ,  $p_x$ ) as arising from a finite number of distinct ionization events, which

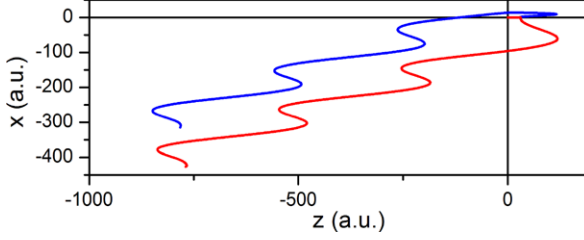
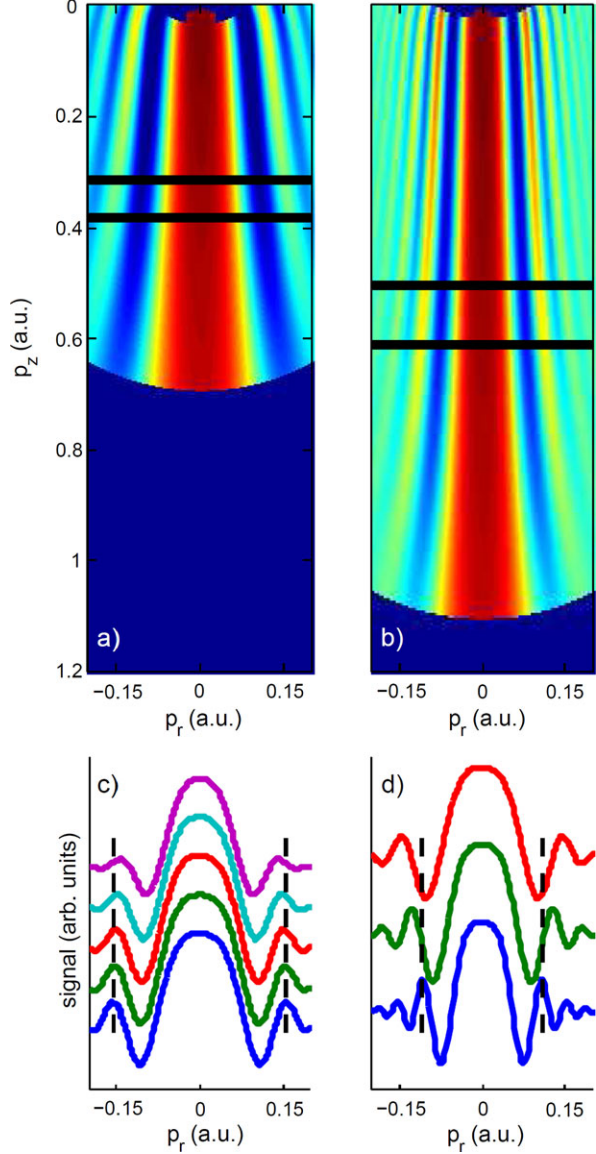


**Fig. 1.7** The role of re-collision in strong-field ionization: two trajectories that lead to the formation of electrons with a final momentum  $p_x = -0.01$  a.u.,  $p_z = -0.46$  a.u. in the ionization of metastable Xe atoms by a  $7 \times 10^{11}$  W/cm<sup>2</sup>, 7  $\mu$ m laser field. The *red trajectory* corresponds to an electron that only weakly interacts with the ionic core, while the *blue trajectory* corresponds to an electron that strongly interacts with ion and undergoes Coulomb focusing. As a result, the radial velocity along the *blue trajectory*, which is initially in the upward direction, is converted into a velocity in the downward direction, allowing this trajectory to interfere on the detector with the *red trajectory*

are accompanied by distinct trajectories that take the electron from the atom or molecule to the detector. When the Coulomb interaction is taken into account during the evaluation of these trajectories, the Coulomb-Corrected SFA (CCSFA) method results [59, 60], which correctly predicts the influence of the Coulomb interaction on the final momentum that the electron acquires and on the phase evolution (in the combined Coulomb and laser field) that the electron experiences on its way to the detector. Hence both the influence of the Coulomb interaction and the possibility for the occurrence of momentum-changing electron-ion re-collisions are automatically included in this method, which therefore allows to correctly predict the location of the holographic interferences. Inspection of the trajectories that are responsible for the emergence of interference maxima and minima illustrates the holographic principle (see Fig. 1.7) and clearly shows that the interference at a given final momentum occurs as a result of the coexistence of non-scattering (i.e. reference) and strongly re-scattering (i.e. signal) trajectories. In addition, the CCSFA method clearly allows to recognize the vital role of the Coulomb interaction, since for the holographic interference to occur it is necessary that the transverse momentum  $p_x$  is reversed when the electron interacts with the ion in the course of the re-collision (see Fig. 1.7).

As an intermediate approach between the application of SFA, which is too simplistic since it neglects re-scattering, and the CCSFA method, which relies on the numerical integration of large numbers of electron trajectories, we have also applied a generalized SFA method. This method does not include the Coulomb interaction, but does include re-collisions of electrons that are driven away from and back towards the ion with zero transverse momentum, and the scattering of these electrons into a spherical wave upon returning to the ion core. The advantage of this method is that it can be treated analytically, and allows to determine that the phase difference  $\Delta\phi$  between the scattered and non-scattered electron waves that causes the holographic interference is dominated by a term,  $\Delta\phi \approx -\frac{1}{2}p_x^2(t_C - t_0^{\text{ref}})$  where,  $t_C$  is the moment of the electron-ion re-collision and  $t_0^{\text{ref}}$  corresponds to the time that the reference wavepacket starts tunneling through the barrier. This expression

**Fig. 1.8** Dependence of the holographic interference on the peak intensity and wavelength of the ionizing laser pulse: (a) interference fringes in the ionization of metastable Xe atoms by a  $7\text{ }\mu\text{m}$  laser field with an intensity  $I = 7.1 \times 10^{11}\text{ W/cm}^2$  (lila),  $5.5 \times 10^{11}\text{ W/cm}^2$  (cyan),  $4.5 \times 10^{11}\text{ W/cm}^2$  (red),  $3.2 \times 10^{11}\text{ W/cm}^2$  (green) and  $1.9 \times 10^{11}\text{ W/cm}^2$  (blue); the contourplot shows the two-dimensional momentum map calculated for  $I = 7.1 \times 10^{11}\text{ W/cm}^2$ ; (b) interference fringes in the ionization of metastable Xe atoms as a function of the laser wavelength while keeping the ponderomotive energy constant. Curves are shown for  $\lambda = 16\text{ }\mu\text{m}$  and  $I = 3.4 \times 10^{11}\text{ W/cm}^2$  (blue), for  $\lambda = 11\text{ }\mu\text{m}$  and  $I = 4.4 \times 10^{11}\text{ W/cm}^2$  (green) and for  $\lambda = 8\text{ }\mu\text{m}$  and  $I = 5.4 \times 10^{11}\text{ W/cm}^2$  (red). In all cases the line-outs are evaluated at  $p_z = 0.5\text{ }p_{z,\text{cut-off}}$ , where the latter value corresponds to the momentum along the polarization axis at the  $2U_p$  cut-off energy; the momentum map shows the result calculated for  $\lambda = 16\text{ }\mu\text{m}$



for  $\Delta\phi$  allows to predict the dependence of the holographic interference pattern on the intensity and wavelength of the laser. The dependence on the intensity of the mid-infrared laser is very modest. When the intensity changes, the values of  $t_C$  and  $t_0^{\text{ref}}$  that lead to the production of a photoelectron with final momentum ( $p_z$ ,  $p_x$ ) only change by very small amounts, suggesting that the interference pattern is very robust with regards to changes in the peak laser intensity and explaining why the holographic interference patterns easily survive the temporal and spatial averaging

that, under experimental conditions, inevitably takes place in a laser focus. These arguments are corroborated by the calculations shown in Fig. 1.8(a), which show the result of generalized SFA calculations for the ionization of metastable Xe atoms by a 7  $\mu\text{m}$  laser with an peak intensity ranging from  $1.9 \times 10^{11}$ – $7 \times 10^{11}$   $\text{W}/\text{cm}^2$  [62]. For a constant value of  $p_z$ , the interference pattern hardly changes as a function of the intensity. This is very different when the wavelength of the ionizing laser is changed. To illustrate this, Fig. 1.8(b) shows a series of calculations where the holographic interference is calculated as a function of the laser wavelength under conditions where the ponderomotive energy (and thus the value of  $p_z$  where the high-energy cut-off is observed in the photoelectron spectrum) stays constant. Figure 1.8(b) clearly shows that with increasing laser wavelength the spacing of the holographic interference fringes narrows, due to the fact that the difference between  $t_C$  and  $t_0^{\text{ref}}$  scales linearly with laser wavelength, leading to a doubling of the phase difference between the reference and signal electron wave at a fixed position in the momentum map [62].

## 1.4 Outlook

It is in the nature of scientific development that advances are often stimulated by the emergence of novel technological capabilities. In this respect, the molecular sciences are no exception. At present, the emergence of intense, short pulse light sources outside the traditional near-infrared to near-UV wavelength range promises the development of novel techniques that address time-dependent dynamics and that do not rely so much on molecular photo-absorption as on diffraction of laser light or the photoelectrons that can be generated using these sources.

On the one hand, at an increasing number of places around the world, XUV/X-ray free electron laser sources are being constructed and coming available, that deliver ultrashort XUV/X-ray laser pulses with unprecedented fluences and peak intensities, that can be used to develop new ways to study time-resolved molecular dynamics based on use of the diffractive properties of energetic photoelectrons that are ejected from time-evolving molecules upon photo-ionization. In the last few years pump-probe protocols have been developed that allow to first dynamically align a molecule of interest, thereby fixing its orientational degrees of freedom in the laboratory frame, before addressing the molecule with a pump pulse that initiates the photo-dynamics of interest and the XUV/X-ray laser pulse that ionizes the molecule and/or fragments resulting from the photo-excitation. In combination with sophisticated 2D or even 3D energy—and angle-resolved photoelectron and—ion detection strategies this promises to lead to the emergence of a novel way of studying photo-chemical events that complements the present absorption-based techniques. There are remaining problems that need to be solved, such as the challenge of adequately synchronizing the FEL light with the output

of the other laser sources that are needed in such an experiment, but rapid advances are being made, and with the more wide-spread use of seeded FEL operation we may expect that in a few years these experiments can be routinely performed. At the same time, continued progress in the capabilities of HHG sources suggests that certain classes of experiments can also be transported to smaller-scale laser laboratories. Some examples of this have been given in the present chapter.

On the other hand, continued progress in the generation of near- and mid-infrared radiation promises the ability to develop novel spectroscopic techniques that are based on the interaction of ponderomotively accelerated photoelectrons with photo-excited and time-evolving molecules. In the present chapter, we have presented one example of this emerging field and have described the presence of holographic interferences in the strong field ionization of metastable Xe atoms using 7  $\mu\text{m}$  laser radiation from a mid-infrared FEL. It is to be expected that the exploration of molecular strong field ionization will soon be investigated in this wavelength range, paving the way for novel spectroscopic techniques for monitoring time-dependent molecular dynamics as well. In doing so, it is very likely that the essence of the results that were obtained so far at an FEL can be transported to smaller-scale laser laboratories. Already, with existing parametric generators and amplifiers it is possible to generate sufficient amounts of radiation in the 3–4  $\mu\text{m}$  wavelength range that studies of strong-field ionization of time-evolving molecules can be confidently attempted. Furthermore, currently on-going developments aimed at the development of high repetition rate optical parametric chirped pulse amplification (OPCPA) laser systems in this wavelength range [63, 64] suggest that the time is not far that sophisticated experimental strategies involving alignment, photo-excitation and mid-infrared strong-field probing of the molecular dynamics can be attempted at 0.1–1 MHz repetition rate, inviting the use of coincident photoelectron-fragment ion detection strategies that allow to measure high quality MFPADs.

The results presented in this chapter represent a starting point of a novel research area that will require significant effort in the coming years, but then also promises to lead to major novel insights into the way that molecular systems behave in response to incident radiation fields.

**Acknowledgements** Apart from the work shown in Fig. 1.5, the present chapter draws heavily from a number of previously published research papers, in particular Refs. [14, 31, 45, 62]. Consequently, the work presented in this chapter would not have been possible without the considerable efforts from a large number of people who contributed to these original publications on the basis of a scientific collaboration. We particularly want to thank Prof. R. Lucchese (Texas A&M University, College Station), M. Lucchini (Politecnico di Milano), Dr. S. Duesterer, Dr. N. Stojanovic, Dr. H. Redlin and the staff at the FLASH FEL in Hamburg, Dr. Ph. Wernet (HZB Berlin), Dr. M. Gensch (DESY Rossendorf), Prof. K. Ueda (Tohoku University, Sendai), Dr. A. van der Meer, Dr. B. Redlich, Dr. G. Berden and Dr. J. Bakker and the staff at the FELICE FEL in Rijnhuizen, Dr. F. Lépine and C. Cauchy (Université de Lyon), Dr. S. Zamith (Université Paul Sabatier, Toulouse), Dr. T. Martchenko (Université Paris 06), Prof. H.G. Muller (AMOLF, Amsterdam), Prof. K. Schafer (LSU, Baton Rouge), Prof. M.Yu Ivanov and Dr. O. Smirnova (MBI, Berlin), Prof. D. Bauer (Rostock University) and Prof. S. Prokhuzhenko (Moscow University).

## References

1. A.H. Zewail, Femtochemistry: atomic-scale dynamics of the chemical bond using ultrafast lasers (Nobel lecture). *Angew. Chem., Int. Ed. Engl.* **39**(15), 2587–2631 (2000)
2. F. Schotte et al., Watching a protein as it functions with 150-ps time-resolved X-ray crystallography. *Science* **300**(5627), 1944–1947 (2003)
3. C. Bressler et al., Femtosecond XANES study of the light-induced spin crossover dynamics in an iron(II) complex. *Science* **323**(5913), 489–492 (2009)
4. M. Woerner et al., Concerted electron and proton transfer in ionic crystals mapped by femtosecond X-ray powder diffraction. *J. Chem. Phys.* **133**(6) (2010)
5. P. Emma et al., First lasing and operation of an angstrom-wavelength free-electron laser. *Nat. Photonics* **4**(9), 641–647 (2010)
6. H.N. Chapman et al., Femtosecond X-ray protein nanocrystallography. *Nature* **470**(7332), 73–77 (2011)
7. H. Ihee et al., Direct imaging of transient molecular structures with ultrafast diffraction. *Science* **291**(5503), 458–462 (2001)
8. P. Baum, D.S. Yang, A.H. Zewail, 4D visualization of transitional structures in phase transformations by electron diffraction. *Science* **318**(5851), 788–792 (2007)
9. N. Gedik et al., Nonequilibrium phase transitions in cuprates observed by ultrafast electron crystallography. *Science* **316**(5823), 425–429 (2007)
10. B.J. Siwick et al., An atomic-level view of melting using femtosecond electron diffraction. *Science* **302**(5649), 1382–1385 (2003)
11. P. Baum, A.H. Zewail, Attosecond electron pulses for 4D diffraction and microscopy. *Proc. Natl. Acad. Sci. USA* **104**(47), 18409–18414 (2007)
12. A. Landers et al., Photoelectron diffraction mapping: molecules illuminated from within. *Phys. Rev. Lett.* **87**(1), e013002 (2001)
13. F. Krasniqi et al., Imaging molecules from within: ultrafast angstrom-scale structure determination of molecules via photoelectron holography using free-electron lasers. *Phys. Rev. A* **81**(3), 033411 (2010)
14. Y. Huismans et al., Time-resolved holography with photoelectrons. *Science* **331**(6013), 61–64 (2011)
15. T. van Oudheusden et al., Compression of subrelativistic space-charge-dominated electron bunches for single-shot femtosecond electron diffraction. *Phys. Rev. Lett.* **105**(26) (2010)
16. T. Brabec, F. Krausz, Intense few-cycle laser fields: frontiers of nonlinear optics. *Rev. Mod. Phys.* **72**(2), 545–591 (2000)
17. P. Agostini, L.F. DiMauro, The physics of attosecond light pulses. *Rep. Prog. Phys.* **67**(6), 813–855 (2004)
18. F. Krausz, M. Ivanov, Attosecond physics. *Rev. Mod. Phys.* **81**(1), 163–234 (2009)
19. P.B. Corkum, Plasma perspective on strong-field multiphoton ionization. *Phys. Rev. Lett.* **71**(13), 1994–1997 (1993)
20. W. Ackermann et al., Operation of a free-electron laser from the extreme ultraviolet to the water window. *Nat. Photonics* **1**(6), 336–342 (2007)
21. M.F. Kling, M.J.J. Vrakking, Attosecond electron dynamics. *Annu. Rev. Phys. Chem.* **59**, 463–492 (2008)
22. E. Goulielmakis et al., Attosecond control and measurement: lightwave electronics. *Science* **317**(5839), 769–775 (2007)
23. P. Emma et al., Femtosecond and subfemtosecond X-ray pulses from a self-amplified spontaneous-emission-based free-electron laser. *Phys. Rev. Lett.* **92**(7) (2004)
24. J.N. Galayda et al., X-ray free-electron lasers-present and future capabilities. *J. Opt. Soc. Am. B, Opt. Phys.* **27**(11), B106–B118 (2010)
25. J. Ullrich et al., Recoil-ion and electron momentum spectroscopy: reaction-microscopes. *Rep. Prog. Phys.* **66**(9), 1463–1545 (2003)
26. H. Stapelfeldt, T. Seideman, Colloquium: aligning molecules with strong laser pulses. *Rev. Mod. Phys.* **75**(2), 543–557 (2003)



27. J.J. Larsen et al., Aligning molecules with intense nonresonant laser fields. *J. Chem. Phys.* **111**(17), 7774–7781 (1999)
28. F. Rosca-Pruna, M.J.J. Vrakking, Experimental observation of revival structures in picosecond laser-induced alignment of I-2. *Phys. Rev. Lett.* **87**(15), 153902 (2001)
29. S. Guerin, A. Rouzee, E. Hertz, Ultimate field-free molecular alignment by combined adiabatic-impulsive field design. *Phys. Rev. A* **77**(4), 041404(R) (2008)
30. O. Ghafur et al., Impulsive orientation and alignment of quantum-state-selected NO molecules. *Nat. Phys.* **5**(4), 289–293 (2009)
31. F. Kelkensberg et al., XUV ionization of aligned molecules. *Phys. Rev. A* **84**(5), 051404 (2011)
32. M.J.J. Vrakking, An iterative procedure for the inversion of two-dimensional ion/photoelectron imaging experiments. *Rev. Sci. Instrum.* **72**(11), 4084–4089 (2001)
33. O. Ghafur et al., A velocity map imaging detector with an integrated gas injection system. *Rev. Sci. Instrum.* **80**(3), 033110 (2009)
34. R.R. Lucchese, K. Takatsuka, V. McKoy, Applications of the Schwinger variational principle to electron molecule collisions and molecular photoionization. *Phys. Rep.* **131**(3), 147–221 (1986)
35. R.R. Lucchese et al., Polar and azimuthal dependence of the molecular frame photoelectron angular distributions of spatially oriented linear molecules. *Phys. Rev. A* **65**(2), 020702 (2002)
36. C.G. Wahlstrom et al., High-order harmonic-generation in rare-gases with an intense short-pulse laser. *Phys. Rev. A* **48**(6), 4709–4720 (1993)
37. P. Colosimo et al., Scaling strong-field interactions towards the classical limit. *Nat. Phys.* **4**(5), 386–389 (2008)
38. W.Y. Hong et al., Broadband water window supercontinuum generation with a tailored mid-IR pulse in neutral media. *Opt. Lett.* **34**(14), 2102–2104 (2009)
39. I. Wilke et al., Single-shot electron-beam bunch length measurements. *Phys. Rev. Lett.* **88**(12), 124801 (2002)
40. C. Gahl et al., A femtosecond X-ray/optical cross-correlator. *Nat. Photonics* **2**(3), 165–169 (2008)
41. P. Johnsson et al., Characterization of a two-color pump probe setup at FLASH using a velocity map imaging spectrometer. *Opt. Lett.* **35**(24), 4163–4165 (2010)
42. P. Johnsson et al., Velocity map imaging of atomic and molecular processes at the free electron laser in Hamburg (FLASH). *J. Mod. Opt.* **55**(16), 2693–2709 (2008)
43. A. Rouzee et al., Angle-resolved photoelectron spectroscopy of sequential three-photon triple ionization of neon at 90.5 eV photon energy. *Phys. Rev. A* **83**(3) (2011)
44. L. Nugent-Glandorf et al., Ultrafast time-resolved soft X-ray photoelectron spectroscopy of dissociating Br-2. *Phys. Rev. Lett.* **87**19(19), 193002 (2001)
45. N. Berrah et al., Non-linear processes in the interaction of atoms and molecules with intense EUV and X-ray fields from SASE free electron lasers (FELs). *J. Mod. Opt.* **57**(12), 1015–1040 (2010)
46. A. Rouzée et al., Towards imaging of ultrafast molecular dynamics using FELs. *J. Phys. B* **46**, 164029 (2013)
47. T. Kanai, S. Minemoto, H. Sakai, Quantum interference during high-order harmonic generation from aligned molecules. *Nature* **435**(7041), 470–474 (2005)
48. J. Itatani et al., Tomographic imaging of molecular orbitals. *Nature* **432**(7019), 867–871 (2004)
49. O. Smirnova et al., High harmonic interferometry of multi-electron dynamics in molecules. *Nature* **460**(7258), 972–977 (2009)
50. H.J. Worner et al., Following a chemical reaction using high-harmonic interferometry. *Nature* **466**(7306), 604–607 (2010)
51. M. Spanner et al., Reading diffraction images in strong field ionization of diatomic molecules. *J. Phys. B, At. Mol. Opt. Phys.* **37**(12), L243–L250 (2004)
52. M. Meckel et al., Laser-induced electron tunneling and diffraction. *Science* **320**(5882), 1478–1482 (2008)

53. C. Nicole et al., Photoionization microscopy. *Phys. Rev. Lett.* **88**(13), 133001 (2002)
54. F. Lepine et al., Atomic photoionization processes under magnification. *Phys. Rev. A* **70**(3), 033417 (2004)
55. J. Itatani et al., Attosecond streak camera. *Phys. Rev. Lett.* **88**(17), 173903 (2002)
56. R. Kienberger et al., Atomic transient recorder. *Nature* **427**(6977), 817–821 (2004)
57. H.G. Muller, An efficient propagation scheme for the time-dependent Schrodinger equation in the velocity gauge. *Laser Phys.* **9**(1), 138–148 (1999)
58. H.R. Reiss, Effect of an intense electromagnetic field on a weakly bound system. *Phys. Rev. A* **22**(5), 1786–1813 (1980)
59. S.V. Popruzhenko, D. Bauer, Strong field approximation for systems with Coulomb interaction. *J. Mod. Opt.* **55**(16), 2573–2589 (2008)
60. S.V. Popruzhenko, G.G. Paulus, D. Bauer, Coulomb-corrected quantum trajectories in strong-field ionization. *Phys. Rev. A* **77**(5), 053409 (2008)
61. W. Becker et al., Above-threshold ionization: from classical features to quantum effects. *Adv. At. Mol. Opt. Phys.* **48**, 35–98 (2002)
62. Y. Huismans et al., Scaling laws for photoelectron holography in the mid-infrared wavelength regime. *Phys. Rev. Lett.* **109**, 013002 (2012)
63. O. Chalus et al., Six-cycle mid-infrared source with 3.8  $\mu\text{J}$  at 100 kHz. *Opt. Lett.* **35**(19), 3204–3206 (2010)
64. C. Erny et al., High-repetition-rate optical parametric chirped-pulse amplifier producing 1- $\mu\text{J}$ , sub-100-fs pulses in the mid-infrared. *Opt. Express* **17**(3), 1340–1345 (2009)
65. A. Rouzée, Thesis. University of Burgundy (2007)

Ultrafast Phenomena in Molecular Sciences

Femtosecond Physics and Chemistry

de Nalda, R.; Bañares, L. (Eds.)

2014, XVII, 287 p. 122 illus., 67 illus. in color.,

Hardcover

ISBN: 978-3-319-02050-1